Structure and Magnetism of $La_4Mn_5Si_4O_{22}$ and $La_4V_5Si_4O_{22}$: Two New Rare-Earth Transition Metal Sorosilicates

C. Gueho,[†] D. Giaquinta,*,[†] J. L. Mansot,[‡] T. Ebel,[†,§] and P. Palvadeau[†]

Institut des Matériaux, Chimie des Solides et Physique Cristalline, UM CNRS 110, 2, rue de la Houssinière, 44072 Nantes CEDEX 03, France

Received July 8, 1994. Revised Manuscript Received January 24, 1995[⊗]

Two new layered silicates, $La_4Mn_5Si_4O_{22}$ and $La_4V_5Si_4O_{22}$, have been prepared and their structures determined. $La_4Mn_5Si_4O_{22}$ and $La_4V_5Si_4O_{22}$ crystallize in the monoclinic space group $C2/m$: $a = 14.024(2)$, $b = 5.571(2)$, $c = 11.703(2)$ Å, $\beta = 114.34(4)°$ with $Z = 2$ formula units per cell and $a = 13.510(3)$, $b = 5.605(1)$, $c = 11.114(2)$ Å, $\beta = 100.45(3)°$ with $Z = 2$ formula units per cell, respectively. The structures were determined by single-crystal X-ray diffraction and refined to residuals of $R = 2.73\%$ and 3.82%, respectively. The manganese compound crystallizes in the perrierite structure while the vanadium compound crystallizes in the related chevkinite structure. Both perrierite and chevkinite display nearly eclipsed sorosilicate groups which separate rutile-like sheets of edge-shared transition metal–oxygen octahedra from single, isolated transition metal–oxygen octahedra. Metal–metal distances within the rutile-like sheet are on the order of 2.8 Å in both compounds, approximately R_c, the critical metal–metal distance defined by Goodenough for appreciable metal–metal interactions and electronic delocalization. Preliminary magnetic data are also presented.

Introduction

The synthesis and study of low-dimensional compounds have received a great deal of focus in recent years in light of their often unusual and anisotropic physical properties.[1–5] The variety of low-dimensional magnetic and electronic interactions that have been discovered makes the study of chain or layered transition-metal compounds especially fruitful, particularly for reduced and multivalent transition-metal systems. Recently, the study of oxophosphate and oxosilicate systems has produced many interesting examples of quasi-low-dimensional systems in which one-dimensional chains or two-dimensional sheets are located between and isolated by phosphate or silicate groups, respectively.[6–9] In an effort to prepare new, interesting layered oxides, we have pursued the synthesis and characterization of reduced, first-row transition-metal oxosilicates. During these investigations, we have prepared two new, layered sorosilicates (silicates with Si_2O_7 groups) with multivalent manganese and vanadium. These compounds are isostructural with perrierite and chevkinite, respectively, naturally occurring minerals from the epidote family of silicates.[8,10–13] The manganese compound $La_4Mn_5Si_4O_{22}$, with the perrierite structure, contains three oxidation states of manganese, 2+, 3+, and 4+; the vanadium compound $La_4V_5Si_4O_{22}$, with the chevkinite structure, has multivalent vanadium(III/IV). The main structural feature of both of these new silicates is the rutile-like layer of edge-shared octahedra with metal–metal distances on the order of 2.8 Å.

Experimental Section

Synthesis and Characterization Techniques. A redox reaction of $LaCl_3$, MnO_2, and SiO_2 resulted in long, dark needles of $La_4Mn_5Si_4O_{22}$, $MnCl_2$, and chlorine gas according to the following formula:

$$7MnO_2 + 4LaCl_3 + 4SiO_2 \rightarrow La_4Mn_5Si_4O_{22} + 2MnCl_2 + 4Cl_2(g)$$

The reaction mixture was heated in a sealed quartz tube with a volume of approximately 10 mL at 850 °C for 10 days. Chlorine gas was observed in the tubes following synthesis. On the basis of the volume of the tube, the reaction scale was chosen to avoid explosions. Only slight tube attack was noted as a clouding of the quartz where the reactants were in contact with the tube. The resulting product was stirred in alcohol to free needles of $La_4Mn_5Si_4O_{22}$ from the $MnCl_2$ matrix.

Shiny, black crystals of $La_4V_5Si_4O_{22}$ were grown from stoichiometric amounts of the oxides in a KCl flux, with a flux-

---

[†] Chimie des Solides.

[‡] Physique Cristalline.

[§] Permanent address: Anorganisch-Chemisches Institut, Universität Münster, Wilhelm-Klemm-Strasse 8, D-48149 Münster, Germany.

[⊗] Abstract published in *Advance ACS Abstracts,* February 15, 1995.

(1) *Magnetic Properties of Layered Transition Metal Compounds*; deJongh, L. J., Ed.; Kluwer Academic Publishers: Dordrecht, 1990; Vol. 9.
(2) Greenblatt, M. *Chem. Rev.* **1988**, *88*, 31–53.
(3) Raveau, B.; Michel, C.; Hervieu, M.; Groult, D. *Crystal Chemistry of High-T_c Superconducting Copper Oxides*; Springer-Verlag: Berlin, 1991; Vol. 15.
(4) *Crystal Chemistry and Properties of Materials with Quasi-One Dimensional Structures*; Rouxel, J., Ed.; D. Reidel Publishing Co.: Dordrecht, 1986; Vol. 291, pp 263–266.
(5) Rouxel, J.; Meerschaut, A.; Gressier, P. *Synth. Met.* **1989**, *34*, 597–607.
(6) Haushalter, R. C.; Wang, Z.; Thompson, M. E.; Zubieta, J.; O'Connor, C. J. *J. Solid State Chem.* **1994**, *109*, 259–264.
(7) Serra, D. L.; Hwu, S.-J. *J. Solid State Chem.* **1992**, *101*, 32–40.
(8) Wang, S.; Hwu, S.-J. *J. Am. Chem. Soc.* **1992**, *114*, 6920–6922.
(9) Benbertal, D.; Mosset, A.; Trombe, J. C. *Mater. Res. Bull.* **1994**, *29*, 47–54.
(10) Bonatti, S. *Am. Mineral.* **1959**, *44*, 115–137.
(11) Calvo, C.; Faggiani, R. *Am. Mineral.* **1974**, *59*, 1277–1285.
(12) Gottardi, G. *Am. Mineral.* **1960**, *45*, 1–14.
(13) Ito, J.; Arem, J. E. *Am. Mineral.* **1971**, *56*, 307–319.

0897-4756/95/2807-0486$09.00/0 © 1995 American Chemical Society

Table 1. Crystallographic Data and Experimental Details for $La_4Mn_5Si_4O_{22}$ and $La_4V_5Si_4O_{22}$

empirical formula	$La_4Mn_5Si_4O_{22}$	$La_4V_5Si_4O_{22}$
formula weight (g/mol)	1294.66	1274.70
crystal system	monoclinic	monoclinic
space group	*C*2/*m* (No. 12)	*C*2/*m* (No. 12)
lattice parameters:		
a (Å)	14.024(2)	13.510(3)
b (Å)	5.571(2)	5.605(1)
c (Å)	11.703(2)	11.114(2)
β (deg)	114.34(4)	100.45(3)
vol (Å^3)	833.06	827.63
Z	2	2
temp (K)	294	294
color and habit	black-brown needle	black needle
crystal dimensions (mm)	0.60 × 0.03 × 0.13	0.30 × 0.03 × 0.03
D_{calc} (g/cm^3)	5.161	5.115
diffractometer	Enraf-Nonius CAD4	Siemens P4
radiation	Mo Kα (λ = 0.710 73 Å)	Mo Kα (λ = 0.710 73 Å)
μ(Mo Kα) (cm^{-1})	139.9	131.8
scan type	ω	ω
F_{000}	1170	1150
$2\theta_{max}$ (deg)	35	35
no. of reflections measured	5329	1369
no. of observations (I > 3.00 σ(I))	1618	874
no. of variables	98	101
corrections:		
Lorentz–polarization		
absorption		
secondary extinction	9.18(1) E-08	1.53(4) E-04
residuals: *R*; R_w	0.026; 0.029[a]	0.038; 0.040[c]
goodness of fit indicator	1.77[b]	0.63[b]
max peak in final diff map (e$^-$/Å^3)	1.05	2.26

[a] $R = \sum||F_o| - |F_c||/\sum|F_o|$ and $R_w = \sqrt{[\sum(w||F_o| - |F_c||^2)/\sum(w|F_o|^2)]}$; w = unit weights. [b] $S = \sqrt{[\sum(w||F_o| - F_c||^2)/(M - N)]}$; M = number of observations; N = variables. [c] $R = \sum||F_o| - |F_c||/\sum|F_o|$ and $R_w = \sum(||F_o| - |F_c||\sqrt{w})/\sum(|F_o|\sqrt{w})$; $w = 1/\sigma^2(F_o) + 0.005412F_o^2$.

Table 2. Atomic Coordinates and U_{eq} Parameters for $La_4Mn_5Si_4O_{22}$ and $La_4V_5Si_4O_{22}$

atom	Wyckoff	*x*	*y*	*z*	U_{eq}
La1	4i	0.23687(2)	0	0.26062(3)	0.0074(1)
La2	4i	0.05169(2)	0	0.74729(3)	0.0082(1)
Mn1	4g	0	0.2517(2)	0	0.0048(1)
Mn2	4i	0.26756(6)	0	0.00102(7)	0.0057(1)
Mn3	2d	0	$^1/_2$	$^1/_2$	0.0094(3)
Si1	4i	0.1653(1)	0	0.5496(1)	0.0058(3)
Si2	4i	0.4130(1)	0	0.7367(1)	0.0052(3)
O1	8j	0.0723(2)	0.2543(6)	0.1800(3)	0.008(1)
O2	8j	0.2899(2)	0.2522(6)	0.1231(3)	0.008(1)
O3	8j	0.3795(2)	0.2692(6)	0.4029(3)	0.012(1)
O4	4i	0.0881(3)	0	0.9897(4)	0.009(1)
O5	4i	0.4165(3)	0	0.0124(4)	0.007(1)
O6	4i	0.4956(3)	0	0.6780(4)	0.015(1)
O7	4i	0.2913(4)	0	0.6384(5)	0.017(1)
O8	4i	0.1385(3)	0	0.4042(4)	0.009(1)
La1	4i	0.35703(8)	0	0.24215(9)	0.0084(3)
La2	4i	0.07088(8)	0	0.24769(9)	0.0096(3)
V1	4f	$^1/_4$	$^1/_4$	$^1/_2$	0.0068(7)
V2A	2c	$^1/_2$	$^1/_2$	$^1/_2$	0.0080(11)
V2B	2d	0	$^1/_2$	$^1/_2$	0.0086(11)
V3	2b	0	$^1/_2$	0	0.0113(12)
Si1	4i	0.2049(4)	$^1/_2$	0.2309(4)	0.0099(14)
Si2	4i	0.3616(4)	$^1/_2$	0.0428(5)	0.0094(12)
O1	4i	0.1457(9)	0	0.4813(9)	0.005(3)
O2	4i	0.1900(10)	0	0.0969(12)	0.012(3)
O3	8j	−0.0214(7)	0.2510(18)	0.3694(7)	0.011(2)
O4	8j	0.2243(6)	−0.2616(16)	0.3141(7)	0.006(2)
O5	4i	0.2870(12)	$^1/_2$	0.1431(13)	0.018(4)
O6	4i	0.1501(10)	$^1/_2$	0.5139(12)	0.014(4)
O7	8j	0.4309(7)	0.2627(19)	0.0842(8)	0.012(2)
O8	4i	0.0915(10)	$^1/_2$	0.1586(14)	0.017(4)

to-reactants ratio of 5:1. The reaction mixture was heated in a sealed quartz tube at 850 °C for 10 days and slow-cooled at 5 °C/h. Slight tube attack was observed as described above. The resulting solid was stirred in water to dissolve the KCl matrix. Single crystals of $La_4Mn_5Si_4O_{22}$ could also be prepared in a KCl flux. Crystals of $La_4Mn_5Si_4O_{22}$ and $La_4V_5Si_4O_{22}$ were obviously twinned, as was apparent under an optical microscope, in the same fashion as that described by Bonatti.[10]

A JEOL JSM-35C scanning electron microscope equipped with a Tracor TN 5500 micro Z system was used for X-ray microanalysis. No Cl or K impurities were detected in the crystals of the title compounds. Magnetic measurements were performed using a Quantum Design MPMS SQUID magnetometer between 2 and 400 K at magnetic flux densities between 1 and 50 kG. Samples were corrected for diamagnetic core constants and for the diamagnetic contribution of the quartz sample holder. Electron energy loss spectroscopy (EELS) was used as an additional technique to probe the oxidation state of the manganese and vanadium atoms. Spectra were recorded with a Philips CM30 transmission electron microscope operating at 200 kV, equipped with a Gatan 666 multichannel spectrometer.

Structural Determination. Single crystals of $La_4Mn_5Si_4O_{22}$ and $La_4V_5Si_4O_{22}$ were analyzed by both Weissenberg and precession photography in order to select a nontwinned crystal suitable for structure determination.

The cell parameters reported in Table 1 were determined and refined by diffraction techniques at 294 K with a least-squares refinement based on 25 reflections with 3 ≤ 2θ ≤ 30° in the case of $La_4Mn_5Si_4O_{22}$ and 24 reflections with 12 ≤ 2θ ≤ 30° for $La_4V_5Si_4O_{22}$. The data were collected using an Enraf-Nonius CAD4 diffractometer and a Siemens P4 diffractometer, respectively, according to data collection parameters listed in Table 1. The space group for both $La_4Mn_5Si_4O_{22}$ and $La_4V_5Si_4O_{22}$ was determined to be *C*2/*m* (No. 12). Data were corrected for Lorentz, polarization, absorption,[14] and secondary extinction. Data reduction and structural solution and refinement were performed using the MOLEN[15] and SHELXTL PLUS[16] packages of structural software, respectively. The atomic scattering factors were those of Cromer and Waber,[17] and the corrections for anomalous dispersions were from Cromer and Waber.[18] Positional and thermal parameters are listed in Table 2, while important interatomic distances and angles are listed in Table 3.

Results and Discussion

Perrierite and Chevkinite. Perrierite and chevkinite are naturally occurring sorosilicates with a resemblance to the epidote family of silicates.[10-13,19] Ito and Arem[13] proposed that these minerals can be represented as $A^{3+}{}_4B^{2+}C^{3+}{}_2Ti^{4+}{}_2O_8(Si_2O_7)_2$. Synthetic compounds exist with A = Ln^{3+}, Ca^{2+}, Sr^{2+}; B = Fe^{2+}, Mg^{2+}, Mn^{2+}; C = Al^{3+}, Fe^{3+} or (M^{2+}, Ti^{4+}) in combinations such that the mean oxidation states are in accord with the chemical formula above. Naturally occurring perrierite and chevkinite were originally reported as crystallizing in space group *C*2/*m*; however, synthetic minerals have been reported in $P2_1/a$. Although the cell volumes of perrierite and chevkinite are similar, in fact, the *a* axes of the two cells are antiparallel and the *c* axis of chevkinite is parallel to (*a* + 2*c*) of perrierite. Thus, $[001]_P = [-102]_{Ch}$ and $\beta_{Ch} = [100] \wedge [-102]_P$, as represented in Figure 1.[13]

---

(14) North, A. C.; Phillips, D. C.; Matthews, F. S. *Acta Crystallogr.* **1968**, *24A*, 351–355.

(15) MOLEN Structure Determination Package; Enraf-Nonius: Delft, The Netherlands, 1990.

(16) SHELXTL PLUS 4.0; Siemens Analytical X-Ray Instruments: Madison, WI, 1989.

(17) Cromer, D. T.; Waber, J. T. In *International Tables for X-ray Crystallography*; The Kynoch Press: Birmingham, UK, 1974; T. 2.2A.

(18) Cromer, D. T.; Waber, J. T. In *International Tables for X-ray Crystallography*; The Kynoch Press: Birmingham, UK, 1974; T. 2.3.1.

(19) Ito, J. *Am. Mineral.* **1967**, *52*, 1094–1104.

Table 3. Important Bond Lengths (Å) and Angles (deg) for $La_4Mn_5Si_4O_{22}$ and $La_4V_5Si_4O_{22}$

$La_4Mn_5Si_4O_{22}$			$La_4V_5Si_4O_{22}$		
		Bond Lengths			
La1	O1×2	2.535(3)	La1	O2	2.525(6)
	O2×2	2.471(3)		O3×2	2.409(3)
	O3×2	2.505(3)		O4×2	2.554(3)
	O4	2.992(4)		O5×2	3.095(5)
	O7×2	3.114(3)		O6	2.731(8)
	O8	2.576(5)		O7×2	2.623(4)
La2	O1×2	2.641(3)	La2	O1	2.610(4)
	O2×2	2.522(3)		O2	2.525(8)
	O3×2	2.660(4)		O3×2	2.444(4)
	O4	2.668(5)		O4×2	2.537(3)
	O6×2	2.917(1)		O7×2	2.720(3)
	O8	2.521(4)		O8×2	3.002(1)
Mn1	O1×2	1.925(3)	V1	O1×2	1.971(3)
	O4×2	1.905(3)		O4×2	2.033(2)
	O5×2	1.856(3)		O6×2	1.971(4)
	Mn1*	2.767(1)		V1*×2	2.803(1)
	Mn1*	2.804(1)		V2A×2	3.657(1)
	Mn2	3.5454(9)			
	Mn2	4.0007(9)			
Mn2	O2×2	1.936(3)	V2A	O1×2	2.017(7)
	O2×2	1.924(3)		O3×4	2.005(3)
	O4	2.464(5)		V2B×2	2.803(1)
	O5	2.037(5)			
	Mn2*×2	2.827(2)			
Mn3	O3×4	2.194(3)	V3	O7×4	2.057(4)
	O6×2	2.109(5)		O8×2	1.960(8)
			V2B	O3×4	1.996(3)
				O6×2	2.006(8)
Si1	O3×2	1.626(4)	Si1	O4×2	1.619(3)
	O7	1.640(4)		O5	1.605(5)
	O8	1.586(5)		O8	1.596(7)
Si2	O1×2	1.643(3)	Si2	O2	1.583(7)
	O6	1.573(6)		O5	1.633(8)
	O7	1.617(4)		O7×2	1.644(4)
		Bond Angles			
O1	Mn1 O1	179.1(2)	O1	V1 O1	180
O4	Mn1 O4	85.3(2)	O4	V1 O4	180
O5	Mn1 O5	83.7(2)	O6	V1 O6	180
O4	Mn1 O5	95.6(2) × 2	O1	V1 O4	94.0(4)
			O1	V1 O6	91.6(4)
			O4	V1 O6	93.7(4)
O2	Mn2 O2	91.7(1)	O3	V2A O3	91.1(5)
O2	Mn2 O2	93.1(1)	O3	V2A O3	180
O2	Mn2 O2	85.8(1)×2	O6	V2A O6	180
O4	Mn2 O5	179.4(2)	O3	V2A O6	93.8(4)×2
			O1	V2B O1	180
			O3	V2B O3	90.9(5)
			O3	V2B O3	180
			O1	V2B O3	93.4(3)×2
O3	Mn3 O3	93.8(1)×2	O7	V3 O7	91.5(5)
O3	Mn3 O3	86.2(1)×2	O7	V3 O7	180
O6	Mn3 O6	180	O8	V3 O8	180
			O7	V3 O8	98.2(4)×2
O3	Si1 O3	104.5(2)	O4	Si1 O4	111.2(6)
O3	Si1 O7	114.4(1)	O4	Si1 O5	106.8(5)
O3	Si1 O8	104.5(2)	O4	Si1 O8	109.2(5)
O7	Si1 O8	113.4(3)	O5	Si1 O8	113.6(8)
Si1	O7 Si2	174.6(4)	Si1	O5 Si2	174.5(9)
O1	Si2 O1	112.8(2)	O2	Si2 O5	117.0(8)
O1	Si2 O6	109.0(2)	O2	Si2 O7	113.7(4)
O1	Si2 O7	105.0(2)	O5	Si2 O7	101.5(5)
O6	Si2 O7	116.1(3)	O7	Si2 O7	108.0(7)

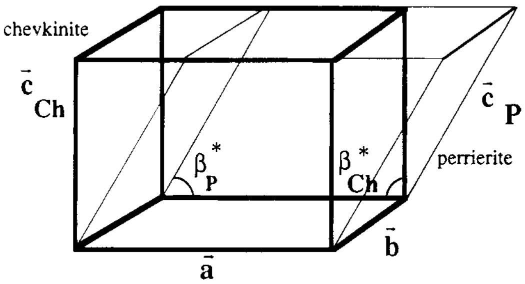

Figure 1. Relationship between the unit cell of perrierite (light lines) and of chevkinite (heavy lines) according to Bonatti.[10]

Notwithstanding the differences in unit cells, the structures (Figure 2) of perrierite and chevkinite are essentially the same. These similarities include layers of rutile-like edge-shared octahedra, M1 (M^{3+}) and M2/M2A, M2B (M^{4+}), located between slabs of sorosilicate groups that separate the isolated M3 octahedra (M^{2+}). Perrierite and chevkinite silicates display an example of layer polymorphism involving a translation of ½ a cell period (see Figure 2b,c).[13] The structural translation occurs on the octahedral layers parallel to (001), the twin plane as reported by Bonatti.[10] These phases are also known to exhibit thermal polymorphism within certain compositional ranges.[13]

Certain structural features of perrierite and chevkinite are distinct, however. These include the Si–O–Si bond angle of the sorosilicate groups and the coordination sphere of the M2 metal site. In the following text, the structures of $Mg_2La_4Ti_3Si_4O_{22}$ (perrierite)[11] and $Mg_2Nd_4Ti_3Si_4O_{22}$ (chevkinite)[11] have been used to illustrate differences in bond lengths in certain metal coordination sites in perrierite, chevkinite, and the title compounds. The sorosilicate groups are bent at the bridging oxygen by an angle of 157° in chevkinite while the bridging angle is 166° in perrierite. Transition metal site M2 is very distorted in perrierite vs chevkinite. In chevkinite the metal–oxygen bonds of M2A and M2B differ by less than 0.1 Å, while in perrierite, the octahedral coordination of M2 is (4 + 1 + 1), with four bonds of similar length, 1.956–1.982 Å, one long bond, 2.421 Å, and one very short bond trans to the former bond, 1.789 Å. This strong interaction between the transition metal and oxygen results in a distortion of the coordination of La1 and effectively the breaking of one lanthanum–oxygen bond and consequently 8-fold coordination of this rare-earth site in perrierite vs 9-fold coordination for the same site in chevkinite.

$La_4Mn_5Si_4O_{22}$. The structure of $La_4Mn_5Si_4O_{22}$ is isostructural with perrierite. Nevertheless, this compound displays the unusual characteristics of three oxidation states of manganese: 2+, 3+, and 4+. Although perrierite often has been reported to have three different oxidation states in unique crystallographic sites, $La_4Mn_5Si_4O_{22}$ is the first perrierite compound in which one metal was responsible for all three oxidation states. Atomic coordinates and isotropic thermal parameters are listed in Table 2, and important bond lengths and angles are listed in Table 3. The rutile slab is formed of alternating chains of undistorted and distorted octahedra noted as Mn1 and Mn2, running parallel to the *b* axis. The Mn3 site is present in isolated octahedra between the sorosilicate groups. The distorted Mn2 octahedra have been attributed to Mn^{3+}, while the undistorted sites have been assigned to Mn^{4+} and Mn^{2+}, with longer Mn–O distances for the latter in agreement with the oxidation state.

A valence-sum calculation using Brown's tables[20] corroborates this oxidation state assignment: Mn1 gives 4.096 valence units (vu); Mn2, 3.152 vu; and Mn3, 2.186

---

(20) Brown, I. D. *Structure and Bonding in Crystals*; Academic Press: New York, 1981.

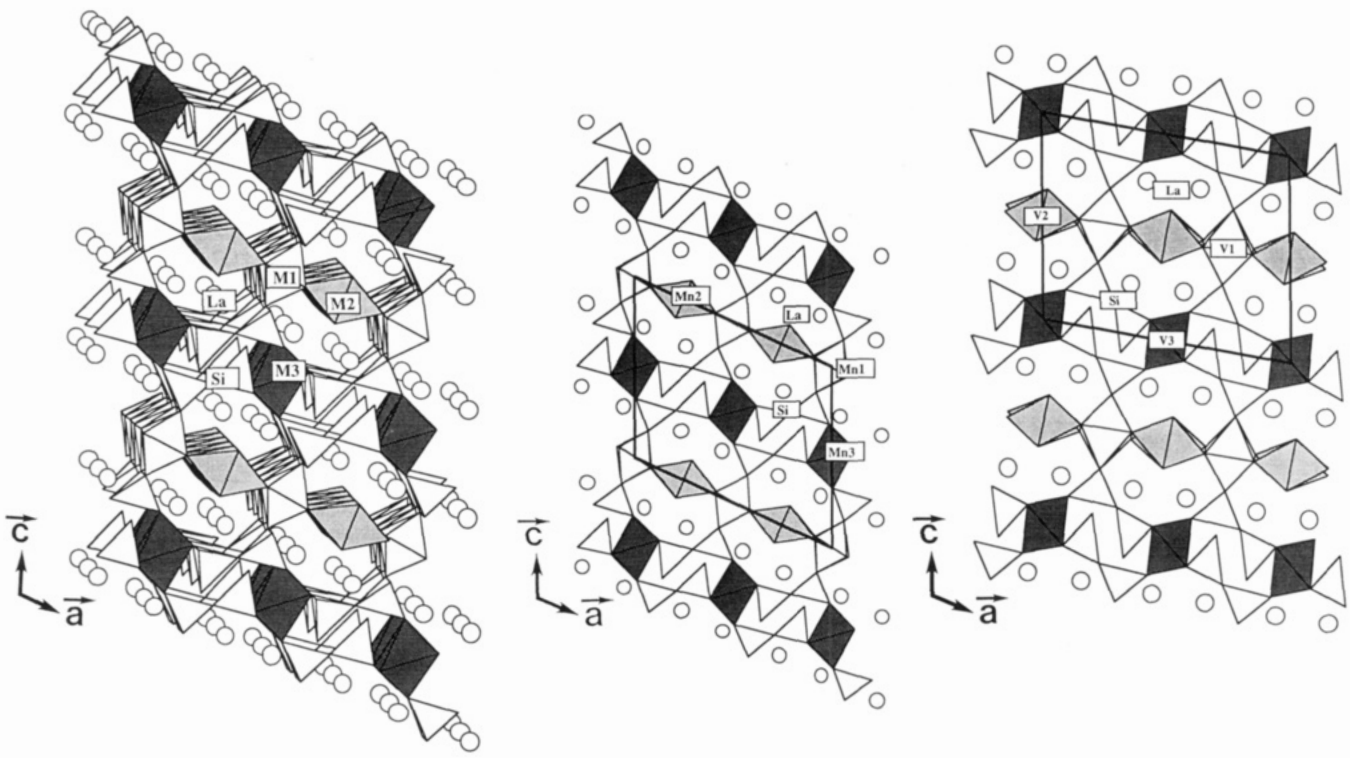

Figure 2. (a, left) Average structure of perrierite and chevkinite in the *ac* plane. Polyhedra are numbered in a general sense, such that the M1 site in this figure is the same site as that represented by Mn1 and V1 in Figure 2b,c. (b, middle) Structure of $La_4Mn_5Si_4O_{22}$ in the *ac* plane. The unit cell of $La_4Mn_5Si_4O_{22}$ is marked for comparison with the unit cell of $La_4V_5Si_4O_{22}$ (Figure 2c). (c, right) Structure of $La_4V_5Si_4O_{22}$ in the *ac* plane. Note that in the chevkinite structure, the site marked V2 is in fact an alternating chain of V2A and V2B sites.

vu. The assignment of oxidation states for manganese and the alternate slab stacking can be illustrated by the structural formula $La_4Mn^{2+}(Si_2O_7)_2(Mn^{3+}Mn^{4+}O_4)_2$. The assignment of Mn^{4+} to the Mn1 site and Mn^{3+} to the Mn2 site is contrary to the reported site assignments in the perrierite structure. This change is believed due to the fact that the distorted coordination of the M2 site in perrierite is more suitable to the Jahn–Teller nature of the Mn^{3+} ion.

The question of the lattice type was addressed by collecting the primitive cell data and inspecting the $h + k = 2n$ reflections to determine whether there existed a weakness or an absence. On the basis of this examination and through the use of photographic methods, it was concluded that the lattice of $La_4Mn_5Si_4O_{22}$ is, in fact, *C* centered. This is in agreement with the previously reported perrierite-like material, $La_4Ti_9Si_4O_{30}$.[8]

The coordination sphere of the distorted transition-metal site (Mn2) within the octahedral sheets of $La_4Mn_5Si_4O_{22}$ is different than the distorted site in perrierite. In $La_4Mn_5Si_4O_{22}$, although there are also four planar bonds of similar length, 1.936 Å × 2 and 1.924 Å × 2, the strong axial interaction seen in perrierite is not present. Instead, although one octahedral distance is very long, 2.464 Å, the trans bond is also significantly longer than the same bond in perrierite at 2.037 Å. This type of octahedral coordination is to be expected for Mn^{3+}, and consequently, although the structure supports a very distorted octahedral coordination, a small rare-earth atom is not necessary for stabilization, as was predicted.[13] The rare earth coordination, thus, is (7 + 1) for La1, and (8 + 2) for La2.

An important structural feature of $La_4Mn_5Si_4O_{22}$ is the metal–metal distances within the rutile layer. Manganese–manganese distances across shared octahedron edges are relatively short: 2.767 and 2.804 Å alternately for the Mn^{4+} chain and 2.827 Å × 2 for the Mn^{3+} chain. These distances are shorter than the Mn–Mn distances observed in the rutile structure of MnO_2,[21] and approach the critical Mn–Mn distance, 2.76 Å, which would indicate that metal–metal interactions may be strong enough to promote delocalization.[22,23] Valence sum calculations, however, would suggest that d electrons are fairly localized.

The presence of three oxidation states of manganese in a single compound is uncommon, reported only in manganese ferrites[24] and in $Mn_{7.5}O_{10}Br_3$;[25,26] thus EELS was employed to verify both the mean oxidation state of manganese and the respective contribution of each valency.[27] Initially, spectra were recorded on well-defined standards in order to establish both the L_3/L_2 ratio and the edge energy position as a function of the oxidation state of manganese. The spectrum of the studied compound is reported in Figure 3. The L_3 edge presents a broad shape with a poorly defined maximum. Therefore, to determine the mean oxidation state of the manganese, the L_3/L_2 white line intensity ratio was used. In this way, a mean oxidation state of manganese,

---

(21) West, A. R. *Solid State Chemistry and Its Applications*; John Wiley & Sons Ltd.: New York, 1984.

(22) Goodenough, J. B. In *Progress in Solid State Chemistry*; Reiss, H., Ed.; Pergamon: New York, 1971; Vol. 5, pp 145–399.

(23) Goodenough, J. B. *Bull. Soc. Chim. Fr.* **1965**, 1200–1207.

(24) Gillot, B.; Legros, R.; Metz, R.; Rousset, A. *Solid State Ionics* **1992**, *51*, 7–9.

(25) Euzen, P.; Leone, P.; Mansot, J. L.; Bonneau, P.; Palvadeau, P. *Mater. Res. Bull.* **1992**, *27*, 1423–1430.

(26) Mansot, J. L.; Leone, P.; Euzen, P.; Palvadeau, P. *Microsc. Microanal., Microstruc.*, in press.

(27) Gueho, C.; Mansot, J. L.; Leone, P.; Giaquinta, D.; Palvadeau, P. *J. Phys. C*, in press.

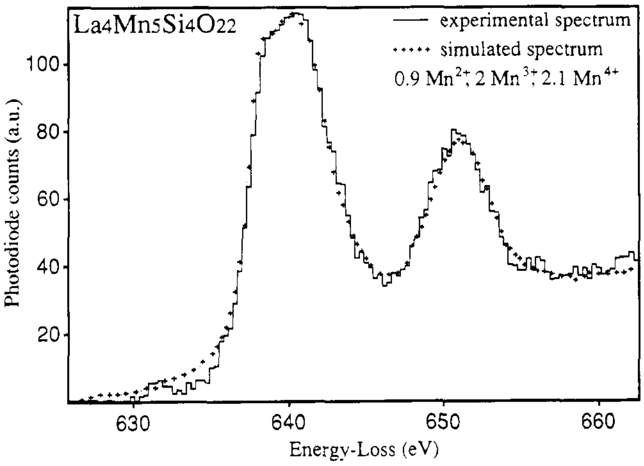

Figure 3. EELS spectrum of $La_4Mn_5Si_4O_{22}$. The experimental spectrum is designated by a solid line, while simulated curve of 0.9 Mn^{2+}/2.0 Mn^{3+}/2.1 Mn^{4+} is designated by (+).

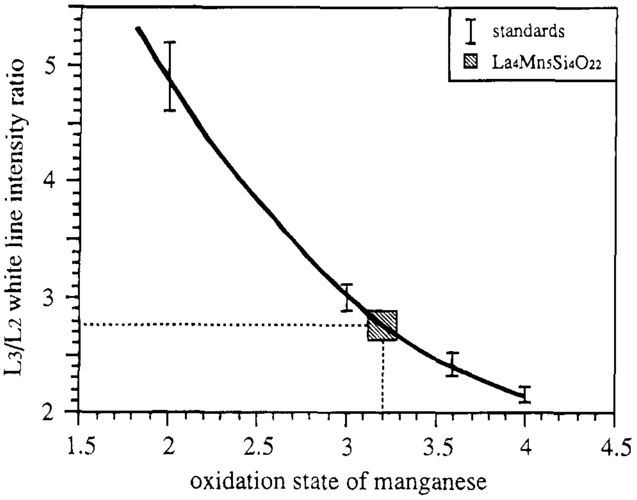

Figure 4. L_3/L_2 white line intensity ratio for manganese plotted vs the oxidation state of manganese. The box designates the position of the mean oxidation state of $La_4Mn_5Si_4O_{22}$. The solid line is added to guide the eye.

+3.25(5), is obtained which corresponds well to the mean oxidation state deduced from the crystal structure refinement, +3.2 (see Figure 4). The best agreement is obtained for the ratio 0.9 Mn^{2+}/2.0 Mn^{3+}/2.1 Mn^{4+}, which is consistent with the structurally determined formulation $La_4Mn^{2+}Mn^{3+}{}_2Mn^{4+}{}_2Si_4O_{22}$. This result is also in agreement with the average oxidation state of manganese determined by thermal gravimetric analysis (TGA).

$La_4V_5Si_4O_{22}$. Unlike the manganese compound, the structure of $La_4V_5Si_4O_{22}$ is isostructural with chevkinite. Atomic coordinates and isotropic thermal parameters are listed in Table 2, and important bond lengths and angles are listed in Table 3. Although the position data and coordination spheres of $La_4V_5Si_4O_{22}$ are virtually the same as in chevkinite, $La_4V_5Si_4O_{22}$ has only two oxidation states of vanadium, unlike the formula of the naturally occurring mineral, $A^{3+}{}_4B^{2+}C^{3+}{}_2Ti^{4+}{}_2O_8(Si_2O_7)_2$. According to valence-bond calculations, none of the sites may be assigned to a specific oxidation state with any degree of confidence. Although many combinations of elements have contributed to the average oxidation state of +3.2 in the literature, $La_4V_5Si_4O_{22}$ is the first example of chevkinite to contain only one element in all four octahedrally coordinated metal sites. The chevkinite and $La_4V_5Si_4O_{22}$ structure, unlike either perrierite or $La_4Mn_5Si_4O_{22}$, displays neither a strong trans effect nor a pronounced Jahn–Teller effect; all of the transition-metal sites are fairly regular.

As with $La_4Mn_5Si_4O_{22}$, the question of whether the correct lattice was primitive or *C* centered was addressed. It was decided, based on preliminary data collection, photography, and the centering condition of both the $La_4Mn_5Si_4O_{22}$ and $La_4Ti_9Si_4O_{30}$ structures, that the lattice of $La_4V_5Si_4O_{22}$ is also *C* centered. Regardless, it was attempted to solve the structure of $La_4V_5Si_4O_{22}$ in the primitive group $P2_1/a$; however, refinement of the structure in this group was less successful than the refinement in the centered group. Weissenberg and precession photographs were employed to determine whether reflections violating the centering condition were present. As in $La_4Mn_5Si_4O_{22}$, no conclusive evidence could be found to imply that the correct crystal lattice of $La_4V_5Si_4O_{22}$ was primitive.

In general, relative bond lengths in $La_4V_5Si_4O_{22}$ are very similar to those seen in the chevkinite structure. As expected, the V3 site, corresponding to the 2+ cations (M3) in chevkinite and $La_4Mn_5Si_4O_{22}$, has the longest average bond lengths. The other sites have very regular bond lengths in chevkinite (never varying from ~2% of the average value) and the same is true in $La_4V_5Si_4O_{22}$. The average vanadium–oxygen bond lengths within the V1 chain of octahedra are very similar to the bond lengths seen in chevkinite, 1.991 Å vs 1.988 Å. In the other chain, where V2A and V2B sites alternate, the bond lengths are similar to chevkinite in a relative sense in that they are essentially equal, but in $La_4V_5Si_4O_{22}$, the bonds are slightly longer at 2.002 and 2.005 Å vs 1.983 and 1.985 Å. The angles in both cases are close to ideal octahedral angles. All vanadium sites within the rutile layer are 2.804 Å from their nearest neighbors within the chain.

The silicon sites are slightly different in $La_4V_5Si_4O_{22}$ than in chevkinite, being more similar to the sorosilicate groups in $La_4Mn_5Si_4O_{22}$. The most noticeable feature is the bend angle of the sorosilicate group. In chevkinite, the angle is often very bent, 157°, while in perrierite it is less so at 165°. In both $La_4Mn_5Si_4O_{22}$ and $La_4V_5Si_4O_{22}$, however, the angle is approximately 175° meaning that the tetrahedra are almost completely eclipsed. The rare-earth coordination is only slightly different in $La_4V_5Si_4O_{22}$ than in the chevkinite structure. In $La_4V_5Si_4O_{22}$, there are 10 oxygen atoms within approximately 3 Å, vs nine in chevkinite. The Jahn–Teller distortion of Mn2 in $La_4Mn_5Si_4O_{22}$ is virtually nonexistent in the V2A and V2B sites of $La_4V_5Si_4O_{22}$; thus there are no compensating long La–O bonds such as those seen in both perrierite and $La_4Mn_5Si_4O_{22}$.

As in the case of $La_4Mn_5Si_4O_{22}$, EELS and TGA were used to verify the mean oxidation state of vanadium. In this case, the EELS analysis was of particular importance since valence bond calculations did not produce satisfying values. Spectra were recorded on well-defined standards in order to establish both the L_3/L_2 ratio and the edge energy position as a function of the oxidation state of vanadium. From the data, Figure 5, a mean oxidation state of +3.25(5) is obtained which corresponds well to the mean oxidation state deduced from the crystal structure refinement, +3.2. Unlike the three oxidation states seen in $La_4Mn_5Si_4O_{22}$, no V^{2+} is present. The best agreement is obtained for the ratio 4 V^{3+}/1 V^{4+}. This assignment is possible if V2A, V2B, or

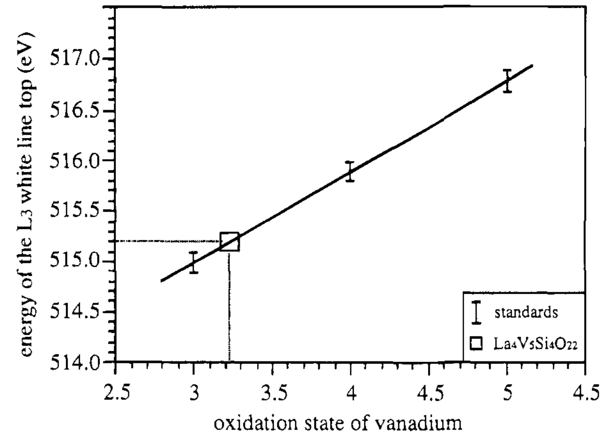

Figure 5. L_3 white-line energy of vanadium plotted vs the oxidation state of vanadium. The box designates the position of the mean oxidation state of $La_4V_5Si_4O_{22}$. The solid line is added to guide the eye.

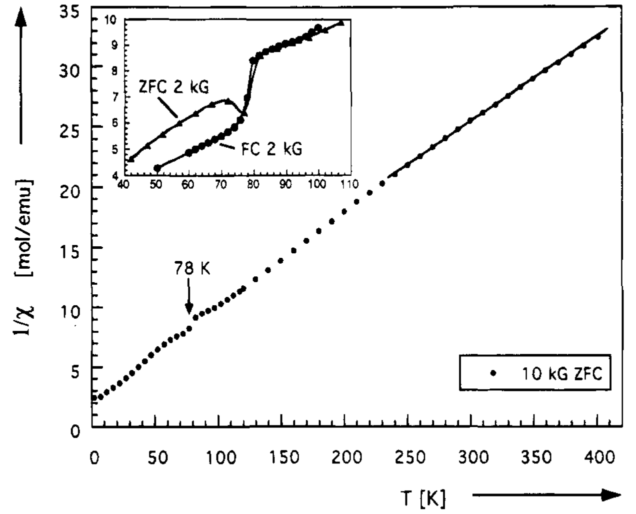

Figure 6. Temperature dependence of the reciprocal susceptibility of $La_4Mn_5Si_4O_{22}$ measured with a magnetic flux density of 10 kG. The line represents the high-temperature least-squares fit according to the Curie–Weiss law. The inset shows the difference between the ZFC and FC values of the reciprocal susceptibility between 40 and 110 K obtained at 2 kG.

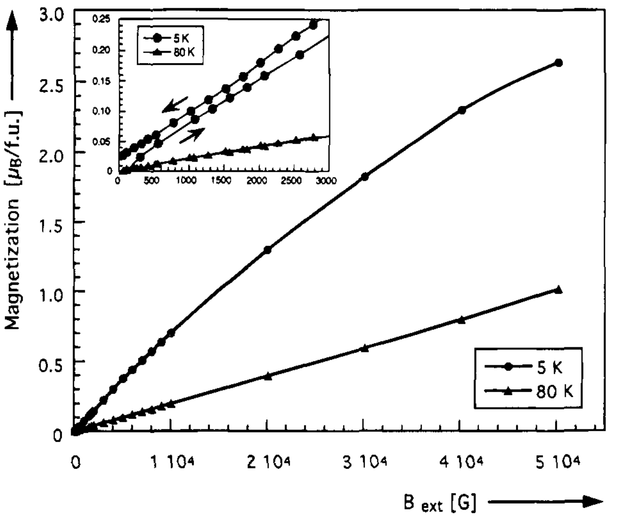

Figure 7. Field dependence of the magnetic moment per formula unit of $La_4Mn_5Si_4O_{22}$ at 5 and 80 K. The inset shows the small hysteresis effect of the magnetic moment observed at 5 K.

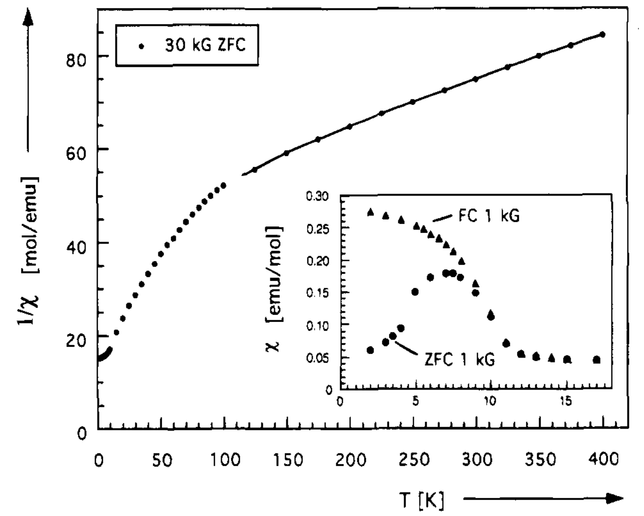

Figure 8. Temperature dependence of the reciprocal susceptibility of $La_4V_5Si_4O_{22}$ measured with a magnetic flux density of 30 kG. The line represents the high-temperature least-squares fit according to the modified Curie–Weiss law. The inset shows the difference between the 1 kG ZFC and FC susceptibility vs temperature data.

V3 is in the 4+ oxidation state while all other sites are 3+. The V3 site is seen as least likely to be in the 4+ oxidation state, considering that this site has the longest average bond lengths. Therefore, since either V2A or V2B, but not both, must be 4+, this creates an alternating V(III)/V(IV) chain within the rutile layer. The exact determination of which site is V(IV), V2A, or V2B, however, is difficult since the bonding of both sites is similar. The average bond length of the V2B site is slightly longer, however. Since the metal–metal distances within the rutile layer are less than the critical V–V distance (2.804 vs 2.94 Å) reported by Goodenough,[22] the mixed-valent state of $La_4V_5Si_4O_{22}$ may be expected to give rise to some electronic delocalization.

Magnetic Characterization. Susceptibility vs temperature and magnetization vs field data for $La_4Mn_5Si_4O_{22}$ and $La_4V_5Si_4O_{22}$ (Figures 6–9) show complicated systems with competitive interactions. Due to the problems associated with the interpretation of powder susceptibility data for a complex magnetic system, the present analysis will thus consist only of descriptions of the different temperature regions.

In the reciprocal susceptibility vs temperature plot (Figure 6), the paramagnetic state of $La_4Mn_5Si_4O_{22}$ above 240 K may be fit with the Curie–Weiss law (1)

$$\chi(T) = C/(T - \Theta) \qquad (1)$$

after correction for 0.1% ferro- or ferrimagnetic impurity determined by the method of Honda and of Owen.[28] The Curie–Weiss constant, $\Theta = -59(1)$ K, is indicative of antiferromagnetic interactions and the experimental magnetic moment, $\mu_{\text{exp}} = 10.64(2)$ μ_B/formula unit according to $\mu_{\text{exp}} = \sqrt{8C}\mu_B$, agrees well with the calculated spin-only high-spin moment of 10.63 μ_B/formula unit, $\mu_{\text{calc}}^2 = 2\mu_{\text{calc}}^2(\text{Mn}^{4+}) + 2\mu_{\text{calc}}^2(\text{Mn}^{3+}) + \mu_{\text{calc}}^2(\text{Mn}^{2+})$ with $La_4Mn_5Si_4O_{22}$ as the formula unit. At intermediate temperatures, interactions, presumably within the rutile sheet, produce an anomaly at 78(2) K (inset, Figure 6). This spike is reproducible between samples, and the temperature of the transition does not change with field, indicating that the boundary between the high-temper-

---

(28) Selwood, P. W. *Magnetochemistry*, 2nd ed.; Interscience Publishers, Inc.: New York, 1956.

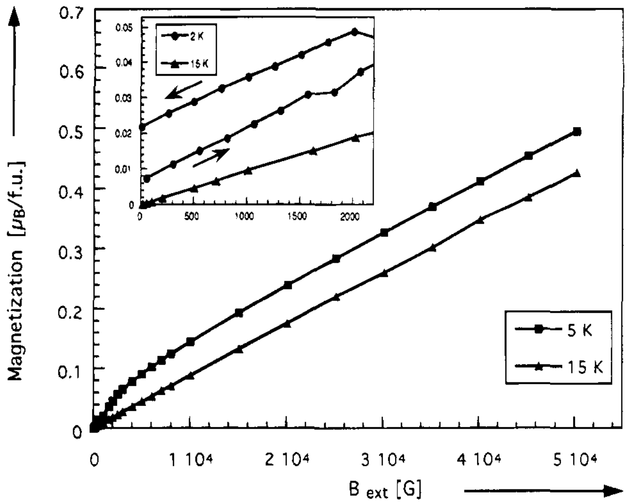

Figure 9. Isothermal magnetization curves at 5 and 15 K. The inset shows the small hysteresis effect of the magnetization obtained at 2 K.

ature state and the low-temperature state does not vary appreciably with field. However the intensity is dependent on the external field with a lower field causing a higher intensity spike. A degree of spin canting may be responsible for the variability of the intensity with external field. Field-cooled (FC) susceptibility data are 30–40% larger than zero-field cooled (ZFC) data below 78 K, supporting the spin canting model. Below 78 K, small saturation effects are seen in the magnetization data (Figure 7), and the slope of the magnetization data is larger at low fields than at higher fields. This is consistent with the observation that the susceptibility anomaly is larger for smaller fields. A remanent magnetization and hysteresis effects are observed in the isothermal magnetization curve below 78 K; however, the value is very small (inset, Figure 7). At temperatures above the spike the magnetization data are linear with no hysteresis effects, characteristic of a paramagnetic state. Thus, the anomaly at 78 K cannot be attributed to an impurity. At temperatures near 10 K, the reciprocal susceptibility begins to flatten. Correct interpretation of this data is difficult, however, for the following reason. We believe the Mn3 octahedral sites remain paramagnetic down to the lowest temperatures measured. These sites are isolated magnetically, being 5.309 or 5.605 Å from the nearest-neighbor Mn1 sites and 5.570 Å from the nearest-neighbor Mn3 sites.

Reciprocal susceptibility vs temperature data for $La_4V_5Si_4O_{22}$ (Figure 8) shows behavior which is quite unlike that seen in $La_4Mn_5Si_4O_{22}$. Field dependence was seen at high temperatures between the 1 and 30 kG data. Data collected at 10 kG, however were identical to that collected at 30 kG; thus 30 kG values were used to compensate for the presence of a possible ferromagnetic impurity. At temperatures above 100 K, the experimental data were fit using the modified Curie–Weiss law (2), where χ_0 is a temperature-independent term.

$$\chi(T) = \chi_0 + C/(T + \Theta) \qquad (2)$$

The TIP term explains the large curvature in the inverse susceptibility at temperatures higher than 100 K and was calculated to $\chi_0 = 3.8(4) \times 10^{-6}$ cm^3/g; 0.76 $\times 10^{-6}$ cm^3/g·V, acceptable for a compound with appreciable metal–metal interactions. The Curie–Weiss constant is large and negative, $\Theta = -193(3)$ K, while the experimental magnetic moment, $\mu_{exp} = 5.76(2)\ \mu_B$/formula unit according to $\mu_{exp} = \sqrt{8C}\mu_B$, is slightly smaller than the calculated moment of 5.92 μ_B/formula unit. The calculated moment of $La_4V_5Si_4O_{22}$ was determined in a similar manner to that described for $La_4Mn_5Si_4O_{22}$. Contribution to the temperature independent susceptibility is expected to cause the observed moment to be smaller than the expected spin-only value, thus the decrease in the effective moment is not unexpected. The behavior of $La_4V_5Si_4O_{22}$ at low temperature is demonstrated in the inset of Figure 8. The susceptibility is very flat until approximately 15 K, where the value increases rapidly to a symmetrical, broad maximum at 8(1) K.

Some field dependency is seen in magnetization measurements below 15 K (Figure 9). As was seen in the case of $La_4Mn_5Si_4O_{22}$, small hysteresis and remanant magnetization effects were observed. FC vs ZFC susceptibility data diverge below 12 K (inset, Figure 8). The low-temperature behavior may perhaps be explained as due to a degree of spin canting or spin-glass-like effects. Further magnetic studies are currently underway in order to clarify the magnetic behavior of both $La_4V_5Si_4O_{22}$ and $La_4Mn_5Si_4O_{22}$.

Conclusions

The structures of two new, layered oxosilicates have been presented. Although the general features of both the perrierite and chevkinite structures are the same, the question of why two different structures exist remains. According to crystal chemistry ideas described by Ito,[13] the two structure types differ only according to combinations of crystal radii. However, according to the method of Ito, both $La_4Mn_5Si_4O_{22}$ and $La_4V_5Si_4O_{22}$ *should* crystallize in the chevkinite structure. Although size factors may play an important role in many of the structures, we believe the key factor contributing to the structures of $La_4Mn_5Si_4O_{22}$ and $La_4V_5Si_4O_{22}$ is electronic. With the exception of $La_4Ti_9Si_4O_{30}$, $La_4Mn_5Si_4O_{22}$ and $La_4V_5Si_4O_{22}$ are the only materials prepared in this general structure type with both (1) one type of transition metal and (2) with the presence of d electrons. We believe the presence of the d electrons determines that $La_4Mn_5Si_4O_{22}$ crystallizes in the perrierite structure and not the ionic radii. The distorted octahedral coordination site in perrierite makes it possible for the Jahn–Teller ion, Mn^{3+}, to crystallize in the M2 site, rather than the M1 site, the location of the 3+ cation in other perrierite structures. The Jahn–Teller distortion thus forces $La_4Mn_5Si_4O_{22}$ to crystallize in the perrierite structure rather than the chevkinite structure due to the stability gained by having Mn^{3+} in a distorted octahedral environment.

Acknowledgment. The authors would like to thank J. Rouxel and C. Payen for valuable discussions.

Supplementary Material Available: Tables of general displacement parameters (2 pages); listings of observed and calculated structure factor amplitudes.

CM9403422